Three-Dimensional Imaging Method Incorporating Range Points Migration and Doppler Velocity Estimation for UWB Millimeter-Wave Radar

Yuta Sasaki, Fang Shang, *Member, IEEE*, Shouhei Kidera, *Member, IEEE*, Tetsuo Kirimoto, *Senior Member, IEEE*, Kenshi Saho, *Member, IEEE*, and Toru Sato, *Member, IEEE*

***Abstract*— High-resolution, short-range sensors that can be applied in optically challenging environments (e.g., in the presence of clouds, fog, and/or dark smog) are in high demand. Ultrawideband (UWB) millimeter-wave radars are one of the most promising devices for the above-mentioned applications. For target recognition using sensors, it is necessary to convert observational data into full 3-D images with both time efficiency and high accuracy. For such conversion algorithm, we have already proposed the range points migration (RPM) method. However, in the existence of multiple separated objects, this method suffers from inaccuracy and high computational cost due to dealing with many observed RPs. To address this issue, this letter introduces Doppler-based RPs clustering into the RPM method. The results from numerical simulations, assuming 140-GHz band millimeter radars, show that the addition of Doppler velocity into the RPM method results in more accurate 3-D images with reducing computational costs.**

***Index Terms*— Multistatic Ultrawideband doppler radar, range points migration (RPM), short-range sensing.**

I. Introduction

SHORT-range, millimeter-wave radar systems have significant advantages including higher spatial resolution and applicability to optically harsh environments (e.g., dark smog, fog, or strong back light) and show promise for various sensing applications such as collision-avoidance sensors for automobiles and watch sensors for elderly or disabled persons living alone. Recently, 140-GHz radar systems have attracted attention, because this frequency minimizes the absorption of moisture vapor, allowing the detection of targets from automobiles in high-moisture environments. Moreover, the size of the transmitting and receiving modules can be considerably reduced, making the actual implementation of the system more flexible. Various studies on 3-D imaging algorithms focused on short-range sensing have been reported, most of which are based on the delay-and-sum (DAS) approach, for example, beamforming, time-reversal algorithms [1], and range migration methods [2] or Kirchhoff migration [3]. However, these studies required high computational costs to obtain full 3-D voxel images and also suffered from limited accuracy for objects with continuous boundaries because of the pointwise target assumption.

To address these issues, a nonparametric, fast, 3-D imaging method called shape estimation algorithm based on boundary scattering transform and Shape Estimation Algorithm based on Boundary scattering transform and Extraction of Directly scattered waves was developed based on reversible transforms between the time delay and the target boundary [4]. However, this method has fundamental drawbacks; for example, it requires a range point (RP) connection procedure during preprocessing, which is difficult in richly interfered situations. The RPs migration (RPM) method was developed as a promising method for solving this problem [5]. This method achieves a batch conversion from RPs (a set of antenna location and observed RPs) to scattering center points with one-to-one correspondence. The RPM method converts each RP (referred to as MainRP) to each scattering center by assessing the focusing degree using all surrounding RPs (called Sub RPs). Notably, this method resolves an inherent paring problem between the range and direction of arrival using a Gaussian kernel-based statistical approach. Thus, the RPM is free from complicated preprocessing involving connecting or paring RPs. This feature confers the significant advantages of both lower computational cost and higher accuracy for locating scattering centers on continuous boundaries, even in richly interfered cases.

Based on the above-mentioned merits, the RPM method has been successfully applied to short-range sensing issues, including the experimental validation [6], the through-the-wall extension [7], or the 3-D ultrasonography imaging issues [8]. In addition, the millimeter radar application assuming 140-GHz band UWB signal has been investigated using a multistatic configuration [9]. The multistatic configuration considerably reduces the time required for data acquisition compared with the radar scanning model, which is necessary

Manuscript received June 27, 2016; revised November 1, 2016; accepted November 10, 2016. Date of publication December 8, 2016; date of current version December 26, 2016. This work was supported by the project 140 GHz band accurate radar system by the Japanese Ministry of Internal Affairs and Communications, Japan.

Y. Sasaki, F. Shang, S. Kidera, and T. Kirimoto are with the Graduate School of Informatics and Engineering, The University of Electro-Communications, Chofu, Tokyo, 1828585, Japan (e-mail: kidera@ee.uec.ac.jp).

K. Saho is with the College of Science and Engineering, Ritsumeikan University, Shiga 5250058, Japan.

T. Sato is with the Graduate School of Informatics, Kyoto University, Kyoto 6068501, Japan.

Color versions of one or more of the figures in this paper are available online at http://ieeexplore.ieee.org.

Digital Object Identifier 10.1109/LGRS.2016.2628909

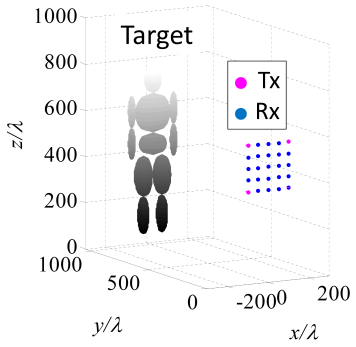

Fig. 1. System model.

for achieving real-time imaging. However, when a sensor receives many reflection echoes, assuming multiple objects or objects with complicated shapes, this method suffers from large computational cost and inaccuracy. This occurs because the RPM assesses a focusing degree using all surrounding RPs (called SubRPs) during the conversion from targeted RPs (called Main RPs) to scattering points, and SubRPs might include unnecessary one. To improve the efficiency and accuracy of the RPM method, this letter introduces a Doppler velocity-based RP clustering algorithm that enhances imaging accuracy by selecting an appropriate set of SubRPs. While Doppler-based data clustering or separation has been demonstrated in lots of studies, there are no investigations for incorporating the RPM for improving both computational efficiency and accuracy. Furthermore, the proposed method can associate a Doppler velocity with each scattering center, which greatly assists in human body recognition as demonstrated in [10]. The results obtained from numerical simulations assuming the 140-GHz band UWB radar system show that the proposed method considerably improves both computational cost and accuracy for 3-D imaging, where the effective imaging points also increases by decomposing the multiple echoes within the same range gate by discriminating the Doppler frequency.

II. System Model

Fig. 1 shows the system model. The model assumes that each target has an arbitrary 3-D shape with a clear boundary and a unique velocity. Antennas are arranged in an array on the $y = 0$ plane to form a multistatic radar configuration. The locations of the transmitting and receiving antennas are defined as $\boldsymbol{L}_T = (X_T, 0, Z_T)$ and $\boldsymbol{L}_R = (X_R, 0, Z_R)$, respectively. For each combination of $\boldsymbol{L}_\mathrm{T}$ and $\boldsymbol{L}_\mathrm{R}$, the recorded electric field is denoted as $s'(\boldsymbol{L}_\mathrm{T}, \boldsymbol{L}_\mathrm{R}, t, \tau)$, where t denotes a fast time and τ denotes a slow time sampled by the pulse repetition interval. $s(\boldsymbol{L}_\mathrm{T}, \boldsymbol{L}_\mathrm{R}, t, \tau)$ is the output of the Wiener filter of $s'(\boldsymbol{L}_\mathrm{T}, \boldsymbol{L}_\mathrm{R}, t, \tau)$ calculated as

$$s(\boldsymbol{L}_\mathrm{T}, \boldsymbol{L}_\mathrm{R}, t, \tau) = \int_{-\infty}^{\infty} W(\omega) S'(\boldsymbol{L}_\mathrm{T}, \boldsymbol{L}_\mathrm{R}, \omega, \tau) \mathrm{e}^{\mathrm{j}\omega t} \mathrm{d}\omega \quad (1)$$

where $S'(\boldsymbol{L}_\mathrm{T}, \boldsymbol{L}_\mathrm{R}, \omega, \tau)$ is the form of Fourier transform of $s'(\boldsymbol{L}_\mathrm{T}, \boldsymbol{L}_\mathrm{R}, t, \tau)$ as to t. $W(\omega)$ is defined as

$$W(\omega) = \frac{S_\mathrm{ref}(\omega)^*}{(1-\eta)S_0^2 + \eta |S_\mathrm{ref}(\omega)|^2} S_0 \quad (2)$$

where $\eta = 1/(1 + (S/N)^{-1})$, and $S_\mathrm{ref}(\omega)$ is the reference signal in the frequency domain, which is the complex conjugate of that of the transmitted signal. S_0 is a constant for dimension consistency. This filter is an optimal mean square error linear filter for additive noises. Since we need to deal with multiple reflection signals from multiple objects, it is quite difficult to determine optimal η, and so an appropriate η is determined empirically. $s(\boldsymbol{L}_\mathrm{T}, \boldsymbol{L}_\mathrm{R}, t, \tau)$ is converted to $s(\boldsymbol{L}_\mathrm{T}, \boldsymbol{L}_\mathrm{R}, R, \tau)$, using $R' = \mathrm{c}t/2$ with the radio wave speed c. Then, the range-Doppler signals as $S(\boldsymbol{L}_\mathrm{T}, \boldsymbol{L}_\mathrm{R}, R', V'_\mathrm{D})$ is obtained by using the 1-D Fourier transform of $s(\boldsymbol{L}_\mathrm{T}, \boldsymbol{L}_\mathrm{R}, R', \tau)$ as to τ. $\boldsymbol{q} \equiv (\boldsymbol{L}_\mathrm{T}, \boldsymbol{L}_\mathrm{R}, R, V_\mathrm{D})^T$ is defined as the RP, which is extracted from the local maxima of $S(\boldsymbol{L}_\mathrm{T}, \boldsymbol{L}_\mathrm{R}, R', V'_\mathrm{D})$ regarding to R' and V'_D as

$$\left.\begin{array}{l} \partial |S(\boldsymbol{L}_\mathrm{T}, \boldsymbol{L}_\mathrm{R}, R', V'_\mathrm{D})| / \partial R' = 0 \\ \partial |S(\boldsymbol{L}_\mathrm{T}, \boldsymbol{L}_\mathrm{R}, R', V'_\mathrm{D})| / \partial V'_\mathrm{D} = 0 \\ |S(\boldsymbol{L}_\mathrm{T}, \boldsymbol{L}_\mathrm{R}, R', V'_\mathrm{D})| \geq \alpha \max |S(\boldsymbol{L}_\mathrm{T}, \boldsymbol{L}_\mathrm{R}, R', V'_\mathrm{D})| \end{array}\right\}. \quad (3)$$

This letter assumes that each RP is assigned to each scattering center on target boundary, and the conversion from the RPs to target boundary points is regarded as an imaging process.

III. Conventional Methods

Various methods for the reconstruction of target shapes in short-range 3-D imaging have been proposed based on the DAS approach, including beam-forming and Kirchhoff migration. Although the DAS-based methods provide accurate images of pointwise targets, they cannot offer sufficient accuracy for nonpointwise targets; moreover, the computational cost becomes enormous in 3-D imaging due to the signal synthesizing approach with all received signals in each voxel evaluation.

The RPM method has been developed to overcome the above-mentioned issues [5], and has been extended to the multistatic observation model [9]. This method assumes that a target boundary point exists on an ellipsoid with focal points $\boldsymbol{L}_T$ and $\boldsymbol{L}_R$ and major radius R. To extract the target point, this method assumes that the actual target boundary point should be included in all the possible intersection points determined by other RPs. To determine a target point $\hat{\boldsymbol{p}}(\boldsymbol{q}_i)$ corresponding to RP $\boldsymbol{q}_i$, this method extracts the optimal intersection points by assessing the spatial accumulation of intersection points calculated by other RPs (called SubRPs) as

$$\hat{\boldsymbol{p}}(\boldsymbol{q}_i) = \underset{\boldsymbol{p}^\mathrm{int}(\boldsymbol{q}_i;\boldsymbol{q}_l,\boldsymbol{q}_m) \in \mathcal{P}_i}{\arg\max} \sum_{(\boldsymbol{q}_j,\boldsymbol{q}_k) \in \mathcal{Q}_\mathrm{all}} g(\boldsymbol{q}_i; \boldsymbol{q}_j, \boldsymbol{q}_k) \times \exp\left\{ -\frac{||\boldsymbol{p}^\mathrm{int}(\boldsymbol{q}_i; \boldsymbol{q}_j, \boldsymbol{q}_k) - \boldsymbol{p}^\mathrm{int}(\boldsymbol{q}_i; \boldsymbol{q}_l, \boldsymbol{q}_m)||}{2\sigma_r^2} \right\}. \quad (4)$$

Here, $p^\mathrm{int}(\boldsymbol{q}_i; \boldsymbol{q}_j, \boldsymbol{q}_k)$ denotes the intersection points among the three ellipsoids, which is determined by the RPs $\boldsymbol{q}_i, \boldsymbol{q}_j$, and $\boldsymbol{q}_k$; $\mathcal{P}_i$ denotes a set of these intersection points; and σ_r is determined considering the spatial density of the accumulated intersection points. $\mathcal{Q}_\mathrm{all}$ denotes a set of all RPs. The weighting

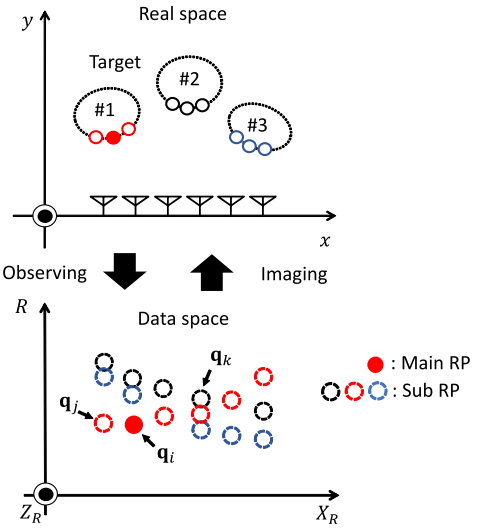

Fig. 2. RPs clustering in RPM scheme.

function $g(\boldsymbol{q}_i; \boldsymbol{q}_j, \boldsymbol{q}_k)$ is defined as

$$g(\boldsymbol{q}_i; \boldsymbol{q}_j, \boldsymbol{q}_k) = s(\boldsymbol{q}_j)\exp\left\{-\frac{D(\boldsymbol{q}_i, \boldsymbol{q}_j)}{2\sigma_D^2}\right\} + s(\boldsymbol{q}_k)\exp\left\{-\frac{D(\boldsymbol{q}_i, \boldsymbol{q}_k)}{2\sigma_D^2}\right\} \quad (5)$$

where σ_D is determined empirically and $D(\boldsymbol{q}_i, \boldsymbol{q}_j)$ denotes the actual separation of the two sets of transmitting and receiving antennas as

$$D(\boldsymbol{q}_i, \boldsymbol{q}_j) = \min(\|\boldsymbol{L}_{\mathrm{T},i} - \boldsymbol{L}_{\mathrm{T},j}\|^2 + \|\boldsymbol{L}_{\mathrm{R},i} - \boldsymbol{L}_{\mathrm{R},j}\|^2, \|\boldsymbol{L}_{\mathrm{T},i} - \boldsymbol{L}_{\mathrm{R},j}\|^2 + \|\boldsymbol{L}_{\mathrm{R},i} - \boldsymbol{L}_{\mathrm{T},j}\|^2). \quad (6)$$

Note that, in (4), the optimal combination of $\boldsymbol{q}_l$ and $\boldsymbol{q}_m$ is determined by full search for all possible combinations.

Notably, in this method, each RP $\boldsymbol{q}_i$ is related to a target point $\boldsymbol{p}(\boldsymbol{q}_i)$ with one-to-one correspondence. The RPM does not require the connection of RPs before processing, allowing the accurate conversion from RPs to target points, even in richly interfered cases. The RPM evaluates the degree of accumulation of the intersection points of ellipsoids for a targeted RP as $\boldsymbol{q}_i$ (named as Main RP) defined by other surrounding RPs (named as SubRPs), $\boldsymbol{q}_j$, and $\boldsymbol{q}_k$ in (4). Fig. 2 shows an example conversion between target points and RPs in a multistatic configuration; the bottom figure shows the cross-sectional view at $(X_\mathrm{T}, Z_\mathrm{T}, Z_\mathrm{R}) = \text{const}$. In this case, each antenna receives a maximum of three RPs, and the RPM converts a Main RP $\boldsymbol{q}_i$ to target boundary point using surrounding all the Sub RPs. However, in the presence of multiple objects, the increasing number of SubRPs seriously increases the computational cost due to the large number of intersection points of the three ellipsoids, which must all be numerically solved. In addition, in the case of multiple objects, the combination of RPs from different targets introduces inaccuracy in the calculation of the actual scattering point.

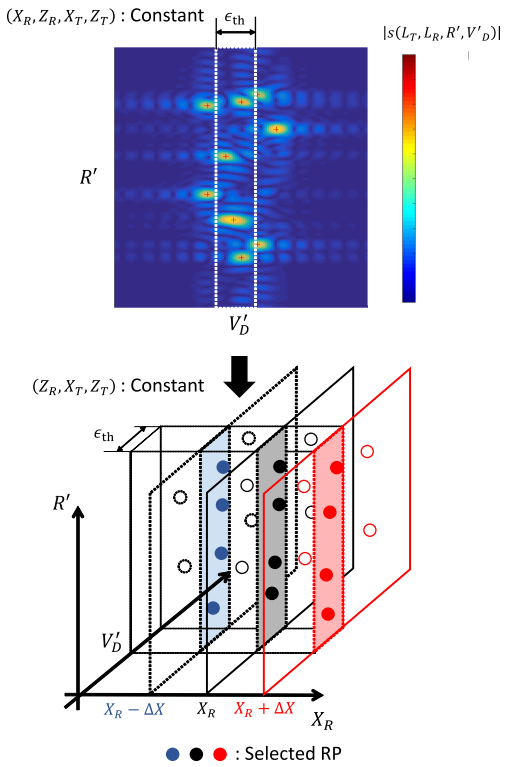

Fig. 3. Example for Doppler-based RP clustering.

IV. Proposed Method

Range clustering represents a promising solution for the above-mentioned issues. In terms of computational efficiency and reconstruction accuracy, the SubRPs are included in the same target cluster of Main RP. That is, if the Main RP caused from the nth target, should be processed using only the SubRPs from the nth target. Fig. 2 shows an example of correctly clustered RPs. As shown in Fig. 2, only a set of SubRPs (red broken circles) is necessary to evaluate Main RP (red solid circle), and other RPs may introduce error into the final image. However, it is generally difficult to cluster the RPs without *a priori* knowledge of target shape or location, because the RPs assuming multiple scatter are overlapped on data space as Fig. 2.

To appropriately cluster SubRPs for each Main RP without *a priori* information about target shape, this letter introduces Doppler-based RPs clustering as a preprocessing step within the RPM method. The new method assumes that a group of RPs generated from an object has almost the same Doppler velocity, and that each RP can be clustered by its associated Doppler velocity before the RPM process. This method introduces the following criteria for $\boldsymbol{q}_i$ (denoted as Main RP) and $\boldsymbol{q}_j$ (denoted as SubRPs):

$$\epsilon(\boldsymbol{q}_i, \boldsymbol{q}_j) \equiv |V_{\mathrm{D},i} - V_{\mathrm{D},j}|. \quad (7)$$

The set of SubRPs that satisfies $\epsilon(\boldsymbol{q}_i, \boldsymbol{q}_j) \leq \epsilon_{\mathrm{th}}$ is denoted as $\mathcal{Q}_i$, and the target point $\hat{\boldsymbol{p}}(\boldsymbol{q}_i)$ is calculated in (4), switching from $\mathcal{Q}_{\mathrm{all}}$ to $\mathcal{Q}_i$. Fig. 3 shows the example of Doppler velocity-based RPs clustering. After extracting range-Doppler map for

TABLE I
DOPPLER VELOCITIES FOR EACH PART OF HUMAN BODY

Doppler velocity	Parts
-1.0 m/s	Right lower arm & Left lower leg
-0.5 m/s	Right upper arm & Left upper leg
0 m/s	Head & Lower and Upper torso
0.5 m/s	Left upper arm & Right upper leg
1.0m/s	Left lower arm & Right lower leg

each antenna combination as $\boldsymbol{L}_{\mathrm{T}}$ and $\boldsymbol{L}_{\mathrm{R}}$, the local maxima of $|S(\boldsymbol{L}_{\mathrm{T}}, \boldsymbol{L}_{\mathrm{R}}, R', V'_{\mathrm{D}})|$ are extracted as Doppler velocity associated RPs. This method confers an additional advantage; multiple RPs within the same range gate but with different Doppler velocities can be decomposed, increasing the effective target points.

The procedure of the proposed method is as follows.

Step 1: Observed data are acquired as the outputs of the Wiener filter $s(\boldsymbol{L}_{\mathrm{T}}, \boldsymbol{L}_{\mathrm{R}}, R', \tau)$.

Step 2: $S(\boldsymbol{L}_{\mathrm{T}}, \boldsymbol{L}_{\mathrm{R}}, R', V'_{\mathrm{D}})$ are obtained by applying the 1-D discrete Fourier transform to $s(\boldsymbol{L}_{\mathrm{T}}, \boldsymbol{L}_{\mathrm{R}}, R', \tau)$ in terms of τ.

Step 3: RPs $\boldsymbol{q}_i$ are extracted from local maxima $|S(\boldsymbol{L}_{\mathrm{T}}, \boldsymbol{L}_{\mathrm{R}}, R', V'_{\mathrm{D}})|$ as to R' and V'_{D}, and a set of all RPs is defined as $\mathcal{Q}_{\mathrm{all}}$.

Step 4: RPs are clustered by the criteria expressed in (7) as $\mathcal{Q}_i$.

Step 5: $\boldsymbol{q}_i$ is converted to a target point $\hat{\boldsymbol{p}}(\boldsymbol{q}_i)$ by the RPM using $\mathcal{Q}_i$ in (4).

Step 6: For each target point $\hat{\boldsymbol{p}}(\boldsymbol{q}_i)$, the associated Doppler velocity $V_{\mathrm{D},i}$ is calculated.

V. EVALUATION IN NUMERICAL SIMULATION

This section evaluates the performance of the original RPM and the newly proposed method using numerical simulation. The transmitting signal forms a pulse-modulated signal with a center frequency of 140 GHz and a 10-dB bandwidth of 10 GHz. The center wavelength λ is 2.1 mm, and the theoretical range resolution in the air is 15 mm. The pulse repetition interval is 37.5 μs, and the number of pulse hits is 56. Thus, the Doppler velocity resolution is 0.5 m/s, and the maximum unambiguous range is 20 m. It assumes that the target is a human body-approximated as an aggregation of 11 ellipsoids corresponding to the head, upper and lower torsos, arms, and legs (Fig. 1). For simplicity, we consider the stepping motion of human body at the same position, where the Doppler velocity of each part is summarized as Table I. The numbers of transmitting and receiving antennas are 4 and 25, respectively, and the minimum array spacing is 50 λ. The received time-series data are generated by geometrical optics (GO) approximation without the consideration of multiple scattering among targets. The GO is the forward solver based on higher frequency approximation, where the dominant propagation path can be determined by the law of reflection in optics [11]. The motivation for applying GO is that it requires much less computational cost compared with other forward solver, such as Finite Difference Time Domain or Method of Moment methods, and we deal with smoothed surface

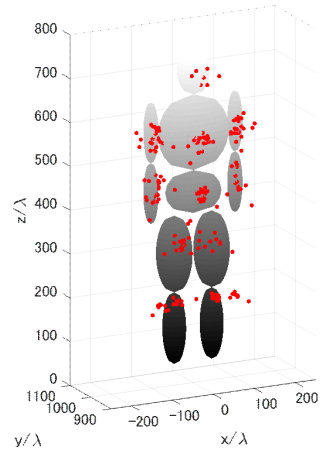

Fig. 4. Scattering center points obtained by the original RPM method in noiseless case.

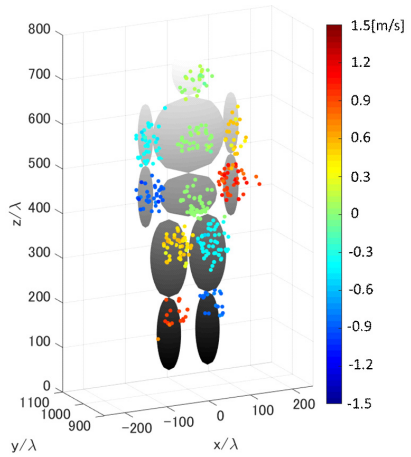

Fig. 5. Scattering center points obtained by the proposed method in noiseless case.

target, the roughness of which is quite larger than the assumed center wavelength (2 mm). Figs. 4 and 5 show the images reconstructed by the original RPM and the proposed methods, respectively. $\epsilon_{\mathrm{th}} = 0.5$ m/s is set in this case. The color of each target point obtained by the proposed method indicates the Doppler velocity. As in Fig. 4, there are some points largely deviated from actual boundary, which are caused by evaluating unnecessary SubRPs in (4). On the contrary, Fig. 5 shows that the proposed method considerably increases the accurately located scattering centers associated with Doppler velocity, compared with those obtained by the original RPM. This improvement occurred, because the RPs corresponding to each part of the human body are correctly clustered by difference in Doppler velocity. It should also be noted that the proposed method decomposes multiple RPs included in the same range resolution based on Doppler velocity; this increases the number of target points, which is another advantage of this method. However, there are nonnegligible deviations from an actual boundary for scattering center points reconstructed by both the original and proposed RPM. These errors are mainly caused by the interferences among reflection signals from different parts in the same range gate, and then, to reduce these errors,

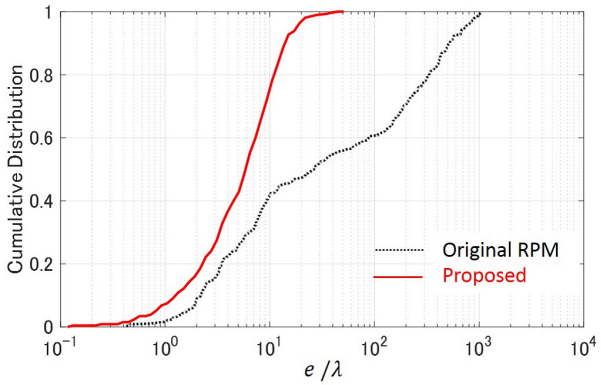

Fig. 6. Cumulative distribution for the reconstruction error e in noiseless case.

TABLE II
ACCURACY ANALYSIS AT $S/N = 30$ dB

	Original RPM	Proposed Method
Average ratio satisfying $e < 10\lambda$	49.2 %	72.1%
Average of $\bar{e}$	12.8 λ (26.9mm)	7.8 λ (16.4mm)

it is promising to introduce a superresolution filter, such as Capon or MUSIC algorithm, which has been demonstrated in [12].

For the quantitative evaluation, the reconstruction error denoted by $e(\boldsymbol{p}_i^{\text{est}})$ is introduced as

$$e\left(\boldsymbol{p}_i^{\text{est}}\right) = \min_{\boldsymbol{p}^{\text{true}}} \|\boldsymbol{p}_i^{\text{est}} - \boldsymbol{p}^{\text{true}}\|_2, \quad (i = 1, 2, \ldots, N_{\text{T}}) \tag{8}$$

where $\boldsymbol{p}_i^{\text{est}}$ and $\boldsymbol{p}^{\text{true}}$ are the locations of the ith estimated point and the true target point (namely, the group of discretized points on ellipsoid surface with sufficiently dense sample in this case), respectively, and N_{T} is the total number of $\boldsymbol{p}_i^{\text{est}}$. Fig. 6 shows the cumulative distribution for $e(\boldsymbol{p}_i^{\text{est}})$ in each method. The numbers of reconstructed points satisfying $e < 10\lambda (= 21\text{mm})$ are 116 (41% of total points) for the original RPM method and 441 (74% of total points) for the new method. The calculation times using a Xeon 3.10-GHz processor are 550 s for original RPM and 160 s for the new method.

Performance evaluations in the noisy cases are described as follows. To simulate a noisy situation, we added white Gaussian noise to the received time-series data. Table II denotes the average ratio for satisfying $e < 10\lambda (= 21\text{mm})$ and that of the mean value of e for the original and new methods in noisy situations at $S/N = 30$ dB, where each quantity is averaged over 100 different noise patterns. S/N is defined as the ratio of the peak instantaneous signal power for all polarization data to the average noise power after applying a matched filter. It should be noted that the above-mentioned definition is the most strict estimation of S/N and considers the locality of signal in both the time and frequency domains, and the signals with $S/N = 30$ dB are practically available by coherent integration procedure, demonstrated in [12]. The results shown in Table II demonstrate that our proposed method still retains more than 70% points satisfying $e < 10\lambda (= 21\text{mm})$, which is improved from that obtained by the original method as less than 50%.

Finally, it should be noted that, in the actual scenario, we should consider the multiple reflection among objects, which would incur an image distortion in any method. However, this kind of distortion is predicted to be not so serious, because the amplitude of higher order multiple reflections would be considerably lower compared with that of direct scattering, and a time gating process for such kind of multiple reflections also could suppress the false image. It is also our future work to discriminate the multiple reflection components by recognizing Doppler velocities.

VI. CONCLUSION

This letter incorporated an RP clustering algorithm based on Doppler velocity into the RPM method to achieve accurate and high-speed 3-D imaging. The numerical simulation assuming the 140-GHz band UWB radar system and the human body imaging issue has demonstrated that the proposed method remarkably enhances the number of accurately reconstructed points associated with the Doppler velocity by decomposing multiple RPs within the same range gate, while reducing the required computational time compared with the conventional RPM method. Further acceleration of this method would be done by introducing more efficient algorithm to search the optimal intersection points in (4), while the present algorithm relies on full search of possible intersection points.

REFERENCES

[1] A. J. Devaney, "Time reversal imaging of obscured targets from multistatic data," *IEEE Trans. Antennas Propag.*, vol. 53, no. 5, pp. 1600–1610, May 2005.
[2] J. M. Lopez-Sanchez and J. Fortuny-Guasch, "3-D radar imaging using range migration techniques," *IEEE Trans. Antennas Propag.*, vol. 48, no. 5, pp. 728–737, May 2000.
[3] F. Soldovieri, A. Brancaccio, G. Prisco, G. Leone, and R. Pierri, "A Kirchhoff-based shape reconstruction algorithm for the multimonostatic configuration: The realistic case of buried pipes," *IEEE Trans. Geosci. Remote Sens.*, vol. 46, no. 10, pp. 3031–3038, Oct. 2008.
[4] T. Sakamoto and T. Sato, "A target shape estimation algorithm for pulse radar systems based on boundary scattering transform," *IEICE Trans. Commun.*, vol. E87-B, no. 5, pp. 1357–1365, Jul. 2004.
[5] S. Kidera, T. Sakamoto, and T. Sato, "Accurate UWB radar three-dimensional imaging algorithm for a complex boundary without range points connections," *IEEE Trans. Geosci. Remote Sens.*, vol. 48, no. 4, pp. 1993–2004, Apr. 2010.
[6] R. Salman and I. Willms, "3D UWB radar super-resolution imaging for complex objects with discontinous wavefronts," in *Proc. IEEE Int. Conf. Ultra-Wideband (ICUWB)*, Oct. 2011, pp. 346–350.
[7] S. Kidera, C. Gao, T. Taniguchi, and T. Kirimoto, "Ellipse based image extrapolation method with RPM imaging for through-the-wall UWB radar," in *Proc. IEEE Int. Geosci. Remote Sens. Symp. (IGARSS)*, Jul. 2015, pp. 385–388.
[8] H. Taki, S. Tanimura, T. Sakamoto, T. Shiina, and T. Sato, "Accurate ultrasound imaging based on range point migration method for the depiction of fetal surface," *J. Soc. Ultrason. Med.*, vol. 42, no. 1, pp. 51–58, Jan. 2015.
[9] Y. Sasaki, S. Kidera, and T. Kirimoto, "Accurate 3-D imaging method based on range points migration for 140GHz-band radar," in *Proc. IEEE Int. Conf. Ubiquitous Wireless Broadband (ICUWB)*, Oct. 2015, pp. 1–5.
[10] Y. Kim and H. Ling, "Human activity classification based on micro-Doppler signatures using a support vector machine," *IEEE Trans. Geosci. Remote Sens.*, vol. 47, no. 5, pp. 1328–1337, May 2009.
[11] V. U. Zavorotny and A. G. Voronovich, "Comparison of geometric optics and diffraction effects in radar scattering from steep and breaking waves," in *Proc. IEEE Int. Geosci. Remote Sens. Symp. (IGARSS)*, Jul. 2007, pp. 1350–1353.
[12] S. Kidera, T. Sakamoto, and T. Sato, "Super-resolution UWB radar imaging algorithm based on extended Capon with reference signal optimization," *IEEE Trans. Antennas Propag.*, vol. 59, no. 5, pp. 1606–1615, May 2011.